Chemical Science

EDGE ARTICLE

View Article Online
View Journal

Check for updates

Cite this: DOI: 10.1039/d6sc03309a

Hydroxyl-radical-specific cascade photogeneration for oxygen-chain photocatalytic therapy

Qiang Liu,[a] Chenxu Yan, *[a] Xie Li,[b] Haiyang Huang,[a] Zheyu Fan,[b] Jizhan Zhang,[a] Weiwei Zhang, [ac] Ping Shi, [b] Yuzheng Zhao,[b] Zhiqian Guo *[ab] and Wei-Hong Zhu [ac]

Received 21st April 2026
Accepted 31st May 2026

DOI: 10.1039/d6sc03309a

rsc.li/chemical-science

The hydroxyl radical ($^{\bullet}OH$), the most potent reactive oxygen species, plays a crucial role in photodynamic therapy (PDT). However, conventional photosensitizers (PSs) that produce $^{\bullet}OH$ through the classical Haber–Weiss pathway suffer from multistep/side reactions, short-lived intermediates, and O_2 dependence, underscoring the demand for direct and selective $^{\bullet}OH$ photogeneration in biological tissues. Here, we report a *de novo* LQM scaffold core allowing the evolution of H_2O into $^{\bullet}OH$ through an unprecedented "H_2O–O_2–$^{\bullet}OH$" oxygen-chain cascade photochemical pathway. The acceptor relocation in D–π–A featured PSs with long-range intramolecular charge transfer can regulate individual oxidation/reduction potentials and fully amplify the electron–hole separation, for the first time achieving $^{\bullet}OH$-specific photogeneration independent of ambient O_2. This generalizable molecular engineering method yields a palette of oxygen-chain PSs that spans the visible and second near-infrared ranges. Our LQM-based oxygen-chain photocatalytic therapy successfully improves therapeutic efficiency in living mice and addresses the long-standing hypoxic challenge of PDT. This study provides a full demonstration of our strategy for the rational design and streamlined PS discovery for $^{\bullet}OH$-specific generation to push the limits of phototherapy in personalized treatment.

Introduction

The hydroxyl radical ($^{\bullet}OH$), the most powerful reactive oxygen species (ROS), can instantaneously obliterate nearly all nearby biomolecules within cancer cells and thereby exhibits exceptional cytotoxicity.[1–7] This unique property makes $^{\bullet}OH$ a potent species in clinical photodynamic therapy (PDT).[8–13] Conventional photosensitizers (PSs), upon excitation with light, transfer energy[14–18] or electrons[19–22] to oxygen (O_2) to generate ROS. While some PSs can produce $^{\bullet}OH$ from O_2 as a substrate, this often occurs *via* the classical Haber–Weiss reaction, involving disproportionation/one-electron transfer reduction of a superoxide anion ($^{\bullet}O_2^-$, as an intermediate) and a subsequent Fenton reaction step.[23–25] Such a multistep process is intrinsically inefficient because of competing side reactions,[26–28] the transient nature of reactive intermediates,[29–31] and its reliance on ambient O_2.[32–36] Water (H_2O), abundant and ubiquitous in biological tissues, is a desirable substrate for PSs. Therefore, there is an urgent need to develop PSs capable of O_2-independent *in situ* $^{\bullet}OH$-specific photogeneration from the water naturally present in biological tissues.

A cascade pathway, involving sequential photocatalytic oxidation of H_2O to generate O_2 and then direct reduction to $^{\bullet}OH$, provides a mechanistic blueprint for self-sustained $^{\bullet}OH$-specific generation. Achieving this "one stone two birds" dual functionality requires two essential prerequisites: long-range electron–hole separation[37–39] for ensuring kinetic feasibility, and individually tailored oxidation/reduction potentials for thermodynamic favorability. Specifically, photogenerated holes must have an oxidation potential > 0.81 V (*vs.* the normal hydrogen electrode) to catalyze the oxidation of H_2O into O_2 ($2H_2O + 4h^+ \rightarrow O_2 + 4H^+$).[40,41] Furthermore, photogenerated electrons with reduction potentials falling within the range from −0.33 V to 0.31 V (refer to $O_2 + e^- \rightarrow {}^{\bullet}O_2^-$ and $O_2 + 3H^+ + 3e^- \rightarrow {}^{\bullet}OH + H_2O$, respectively)[42–44] are required to specifically reduce O_2 into $^{\bullet}OH$. In principle, these criteria delineate the

---

[a] Key Laboratory for Advanced Materials and Joint International Research Laboratory of Precision Chemistry and Molecular Engineering, Shanghai Key Laboratory of Functional Materials Chemistry, Feringa Nobel Prize Scientist Joint Research Center, Institute of Fine Chemicals, Frontiers Science Center for Materiobiology and Dynamic Chemistry, School of Chemistry and Molecular Engineering, East China University of Science and Technology, Shanghai 200237, China. E-mail: chenxuyan@ecust.edu.cn; guozq@ecust.edu.cn

[b] Optogenetics & Synthetic Biology Interdisciplinary Research Center, Shanghai Frontiers Science Center of Optogenetic Techniques for Cell Metabolism, State Key Laboratory of Bioreactor Engineering, School of Pharmacy, East China University of Science and Technology, Shanghai 200237, China

[c] State Key Laboratory of Green Chemical Engineering and Industrial Catalysis, Center of Photosensitive Chemicals Engineering, East China University of Science and Technology, Shanghai 200237, China

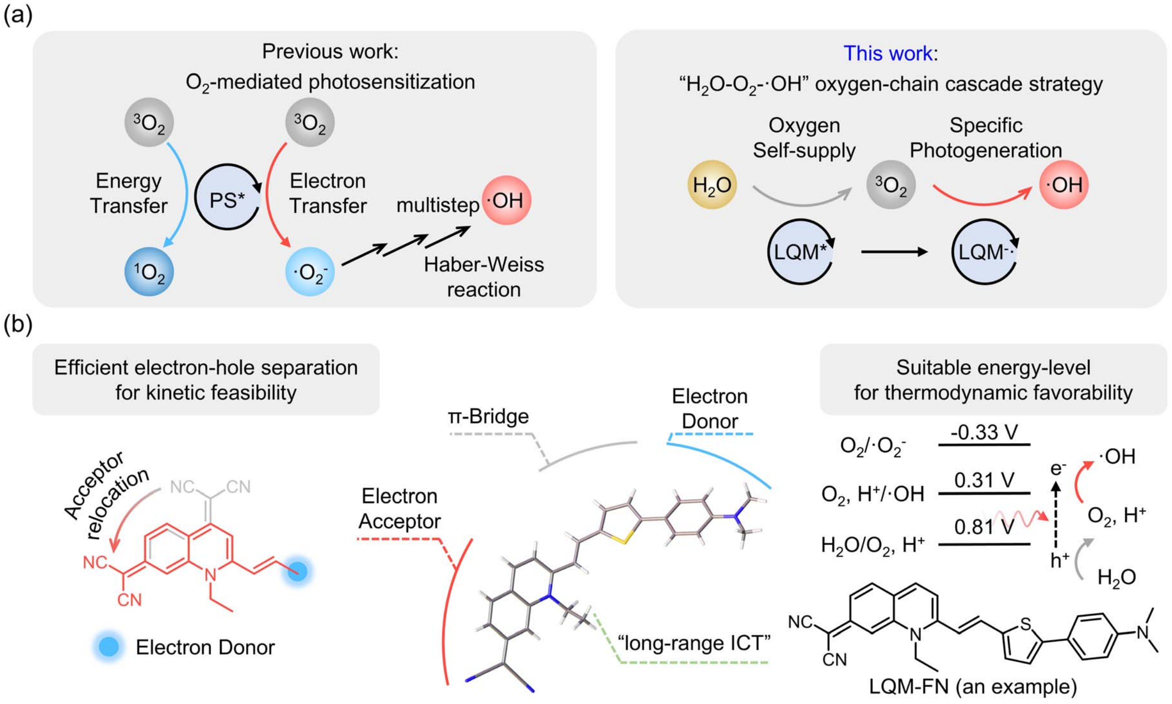

Fig. 1 Hydroxyl-radical-specific cascade photogeneration *via* LQM-based photosensitizers. (a) Schematic illustration of previous work: O_2-mediated nonspecific photosensitization producing $^{\bullet}OH$ *via* the classical Haber–Weiss reaction suffers from multistep/side reactions, short-lived intermediates, and O_2 dependence. This work: evolution of H_2O into $^{\bullet}OH$ through an unprecedented "$H_2O–O_2–{}^{\bullet}OH$" oxygen-chain cascade strategy that integrates oxygen self-supply with hydroxyl-radical-specific photogeneration. (b) *De novo* LQM photosensitizers that orchestrate $H_2O–O_2–{}^{\bullet}OH$ oxygen-chain cascade photochemical reactions by dual regulation: (i) suitable oxidation potentials make it feasible to photocatalytic water splitting to generate O_2, while finely tuned reduction potentials between $O_2/{}^{\bullet}O_2^-$ (−0.33 V) and O_2, $H^+/{}^{\bullet}OH$ (0.31 V) thermodynamically permit selective $^{\bullet}OH$ production; (ii) acceptor relocation with long-range intramolecular charge transfer promotes efficient electron–hole separation (1.82 Å), fulfilling the kinetic requirements for the cascade process. Note: the potential values in panel (b) are determined *versus* the normal hydrogen electrode (NHE) at pH 7.

fundamental requirements for constructing a unique PS capable of $^{\bullet}OH$-specific cascade photogeneration. However, translating these requirements into a practical unimolecular system remains a formidable challenge, and no such platform has been reported to date.

Here, we present a "$H_2O–O_2–{}^{\bullet}OH$" oxygen-chain photogeneration strategy (Fig. 1a) that enables the evolution of H_2O into $^{\bullet}OH$ *via* a consecutive oxidation and electron transfer process. This cascade strategy has, for the first time, achieved $^{\bullet}OH$-specific photocatalytic therapy independent of ambient O_2. We create a new donor–π–acceptor (D–π–A) building block LQM through acceptor relocation, accessible *via* a concise two-step synthesis from commercially available starting materials. As demonstrated, we show that the acceptor relocation within LQM derivatives can lead to an unprecedented $H_2O–O_2–{}^{\bullet}OH$ photochemical pathway (Fig. 1b): (i) suitable oxidation potentials make it feasible to photocatalytically split H_2O to generate molecular O_2, while finely regulated reduction potentials that fall between the potential of $O_2/{}^{\bullet}O_2^-$ (−0.33 V) and O_2, $H^+/{}^{\bullet}OH$ (0.31 V) thermodynamically permit selective $^{\bullet}OH$ generation. (ii) The long-range intramolecular charge transfer facilitates efficient electron–hole separation (1.82 Å), fulfilling the kinetic prerequisites. We expand this strategy to yield a palette of long-wavelength PSs ranging from the visible to the second near-infrared (NIR-II) region. This $^{\bullet}OH$-specific approach effectively solves the long-standing essential issues of PDT, that is, therapeutic efficiency and hypoxic limitation. We thus establish oxygen self-supplying photocatalytic therapy with multiplex *in vivo* imaging. This work presents a pioneering molecular design paradigm for $^{\bullet}OH$-specific photogeneration, providing a promising strategy to improve the treatment of hypoxic solid tumors.

Results and discussion

De novo design of the LQM core *via* acceptor relocation

D–π–A scaffolds, composed of electron-donating and electron-accepting units connected *via* a π-conjugated bridge, inherently promote intramolecular charge transfer (ICT)[45–47] upon photoexcitation. This directional electron migration (from the donor to the acceptor) effectively generates a charge-separated state, thereby suppressing electron–hole recombination and facilitating charge transport or energy utilization.[48–51]

The quinoline-malononitrile (QM) building block has emerged as a versatile D–π–A core with several features, such as high fluorescence brightness and marked photostability.[52,53] Through our established synthesis protocols, QM (with 4-position dicyanomethylene-substitution) can be prepared by reacting malononitrile and 1-ethyl-2-methylquinolinium iodide *via* a Michael addition–elimination reaction (Fig. 2a). In our recent explorations of dye synthesis, commercially available 7-fluoro-2-

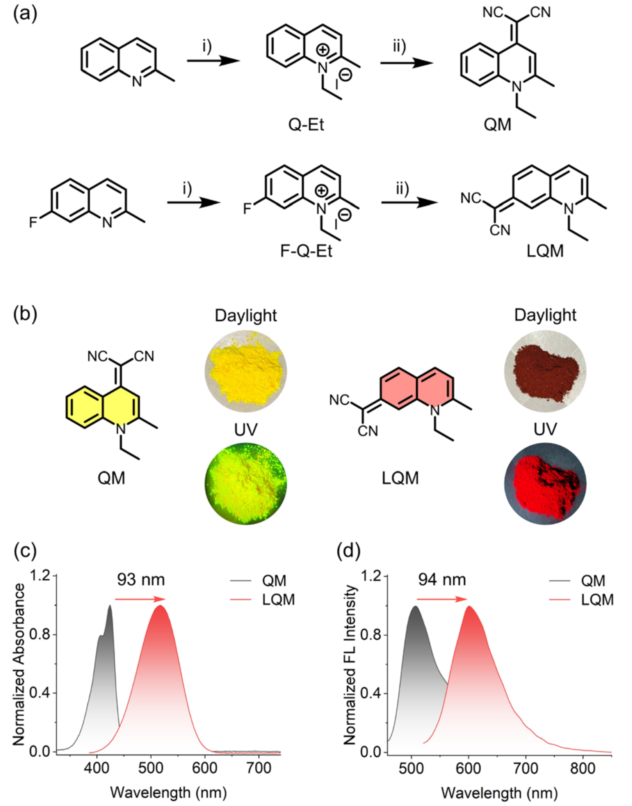

Fig. 2 Red-shifted LQM building block. (a) Synthesis route of QM and LQM: (i) iodoethane, 1,2-dichlorobenzene, 140 °C, 8 h; (ii) malononitrile, sodium ethoxide, ethanol, 25 °C, 24 h. (b) Chemical structures of QM and LQM, accompanied by photographs of QM and LQM under daylight and ultraviolet light. (c) Normalized absorption spectra of QM and LQM in ethanol. (d) Normalized fluorescence spectra of QM ($\lambda_{ex} = 424$ nm) and LQM ($\lambda_{ex} = 500$ nm) in a DMSO/H_2O mixture, v/v = 1 : 9.

methylquinoline served as the starting material, with the fluorine atom at the 7-position enabling nucleophilic substitution. This relocated the malononitrile moiety from the 4-position to the 7-position of the quinoline unit, yielding a new chromophore core, 2-(1-ethyl-2-methylquinolin-7(1*H*)-ylidene)malononitrile, which we termed LQM (Fig. 2a). Compared with QM, this structural alteration in LQM significantly red-shifted both absorption and fluorescence spectra: the maximum absorption wavelength increased from 424 nm to 517 nm (Fig. 2c), producing a visible color transition from yellow to red (Fig. 2b). Correspondingly, the maximum fluorescence emission wavelength exhibited a noticeable red-shift from 507 nm to 601 nm (Fig. 2d). As such, we report an accessible two-step synthesis method for generating a red-shifted quinoline-based chromophoric core (LQM) *via* relocation of the malononitrile moiety.

Constructing a D–π–A featured NIR-II fluorophore library

To achieve effective charge separation, we developed a series of D–π–A fluorophores by introducing electron-donating substituents to the LQM core *via* a Knoevenagel condensation reaction. This reaction utilized the reactive methyl group at the 2-position of the LQM core, enabling robust synthesis of D–π–A fluorophores in excellent yields (up to 71%) on a gram scale. These fluorophores, collectively designated as LQM-Fluors, represent a highly tunable molecular library (Fig. 3a and S1 in the SI). For instance, LQM-FN incorporates the *para*-dimethylaminophenyl group as the electron donor, thiophene as the π-conjugated bridge, and the LQM core as the electron acceptor (Fig. 3a). Within LQM-Fluors, we have synthesized seven representative examples. These highly tunable fluorophores inspired us to further study their spectral diversity.

An obvious feature of LQM-Fluors is their bathochromic-shift optical performance compared to QM-based analogs. Despite sharing identical molecular weights, LQM-FN displayed a significant red shift in maximum absorption wavelength at 608 nm, a 139 nm increase relative to QM-FN (469 nm, Fig. 3a and e). This pronounced shift is primarily ascribed to the relocation of the malononitrile group from the 4-position to the 7-position, transforming the π-conjugation system from bifurcated to linear. Additionally, the maximum absorption wavelengths of LQM-Fluors were strongly correlated with the electron-donating strength of their donor substituents (Fig. 3a). For example, LQM-N (modified with *para*-dimethylaminophenyl) exhibited a maximum absorption wavelength at 585 nm, while LQM-FOO (bearing a strongly electron-donating moiety) showed a markedly red-shifted peak at 624 nm. Fluorescence characterization further revealed that LQM-FOO emitted at 794 nm, achieving a bathochromic shift of 172 nm relative to the parent LQM (Fig. 3f). Notably, benefiting from the broad spectral profiles of D–π–A fluorophores,[54–57] LQM-Fluors showed emission extending into the NIR-II window (Fig. 3f, S2 and S3). Moreover, LQM-Fluors exhibited significantly superior photostability compared with FDA-approved agent indocyanine green (ICG, Fig. S4). These findings highlight how tuning the substituent position of the acceptor unit enhances ICT, offering great promise for bioimaging and phototherapy.

It is well established that, due to the aggregation-caused quenching (ACQ) effect, most fluorophores suffer from severely limited fluorescence intensity and ROS generation efficiency.[58] To assess the aggregation tolerance of LQM-Fluors, we investigated their fluorescence emission properties in H_2O/tetrahydrofuran (THF) mixtures with varying volume fractions (Fig. 3g and S2). The results demonstrated that LQM-Fluors exhibit typical aggregation-induced emission (AIE) characteristics. For instance, both LQM-FN and LQM-FOO showed continuous enhancement in fluorescence intensity with increasing H_2O fraction. Single-crystal X-ray diffraction analysis revealed that LQM-Fluors adopt highly twisted conformations, similar to the AIEgen QM-FN (Fig. 3b–d and S5). In LQM-FN, the dihedral angle between the quinoline and thiophene planes is 43.72(13)°, and the angle between the thiophene and phenyl planes is 10.58(14)°. For LQM-FOO, these angles are 18.07(10)° and 24.73(12)°, respectively. Such twisted geometries effectively suppress intermolecular π–π stacking interactions that typically cause ACQ,[59–62] thereby endowing LQM-Fluors with great potential for high-performance fluorescence imaging and phototherapeutic applications.

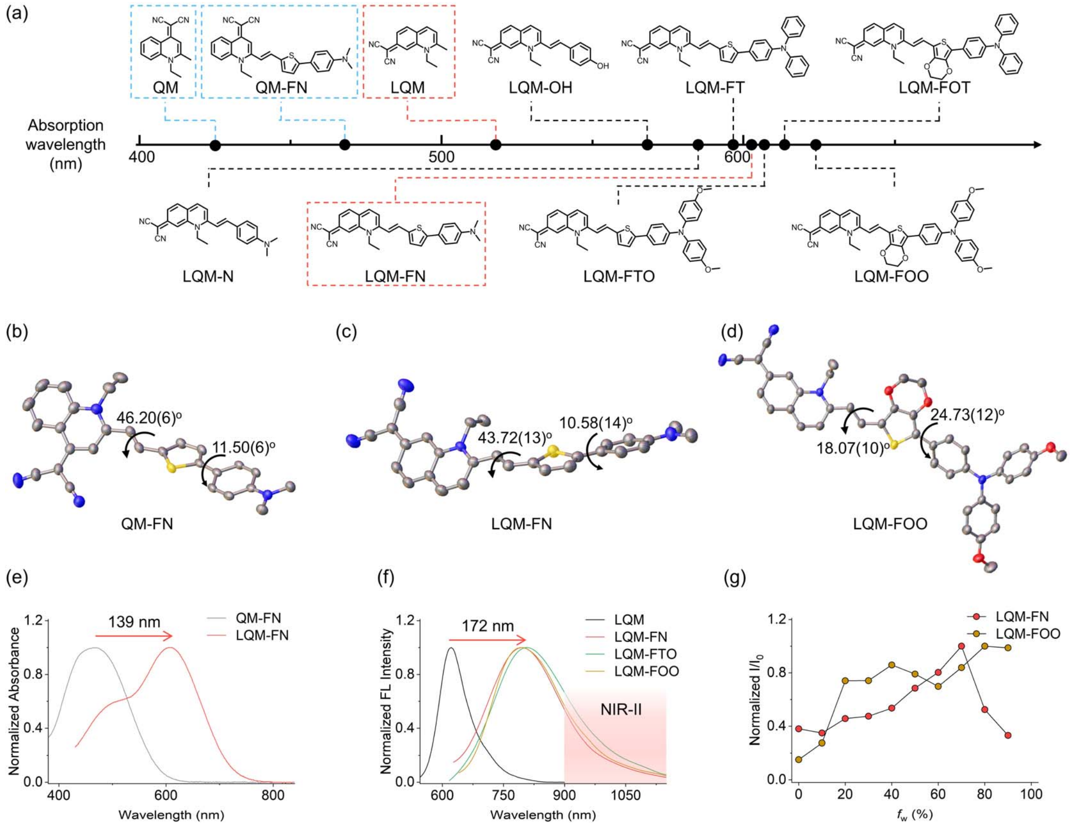

Fig. 3 Panel of LQM-Fluors and their photophysical properties. (a) Chemical structures and maximum absorption wavelengths of QM, QM-FN, and LQM-Fluors in ethanol. (b–d) Single-crystal X-ray structures of QM-FN (b), LQM-FN (c), and LQM-FOO (d). Note: solvent molecules and H atoms are omitted for clarity. (e) Normalized absorption spectra of QM-FN and LQM-FN (10 μM) in ethanol. (f) Normalized fluorescence spectra of LQM ($\lambda_{ex} = 517$ nm), LQM-FN ($\lambda_{ex} = 602$ nm), LQM-FTO ($\lambda_{ex} = 608$ nm), and LQM-FOO ($\lambda_{ex} = 624$ nm, 10 μM) in ethanol. (g) Variation in normalized I/I_0 of LQM-FN ($\lambda_{ex} = 594$ nm, $\lambda_{em} = 813$ nm) and LQM-FOO ($\lambda_{ex} = 625$ nm, $\lambda_{em} = 848$ nm, 10 μM) in a H_2O–THF mixture with varying H_2O fractions (f_w, v/v). I_0 is the emission intensity of different fluorophores in THF.

Hydroxyl radical-specific photogeneration distinct from the classical Haber–Weiss reaction

To evaluate the ROS generation capability of LQM-Fluors, we employed 2′,7′-dichlorodihydrofluorescein as the total ROS indicator (DCFH, a fluorescence-enhancing type indicator). Upon light irradiation, QM-FN induced negligible changes in the fluorescence intensity of DCFH, indicating an absence of ROS generation. In contrast, LQM-Fluors effectively oxidized DCFH, resulting in a continuous increase in fluorescence intensity at 526 nm (Fig. 4a, b and S6), thereby confirming their photoinduced ROS-generating ability. To determine the specific ROS types produced, we utilized 9,10-anthracenediyl-bis(methylene) dimalonic acid (ABDA), dihydroethidium (DHE), and hydroxyphenyl fluorescein (HPF) as selective indicators for singlet oxygen ($^1O_2$), superoxide anion ($^{\bullet}O_2^-$), and hydroxyl radicals ($^{\bullet}OH$), respectively. Chlorin e6 (Ce6) was used as a reference, which is a commercial photosensitizer known to generate lots of $^{\bullet}O_2^-$, a small amount of $^1O_2$, and few $^{\bullet}OH$.[63,64] Compared to Ce6, LQM-Fluors induced negligible spectral changes in ABDA and DHE assays under light exposure (Fig. 4c–f and S6), indicating minimal generation of $^1O_2$ and $^{\bullet}O_2^-$. Furthermore, using methylene blue as a reference photosensitizer further confirmed the negligible generation of $^1O_2$ by LQM-Fluors (Fig. S7). In contrast, a substantial increase in HPF fluorescence was observed upon irradiation (Fig. 4g, h, S6 and S8), demonstrating that $^{\bullet}OH$ is the predominant ROS generated by LQM-Fluors. Given their ability to selectively generate $^{\bullet}OH$, LQM-Fluors were further designated as LQM-based photosensitizers (LQM PSs), including LQM-FN, LQM-FT, LQM-FTO, LQM-FOT, and LQM-FOO.

As established, the classical Haber–Weiss reaction involves redox cycling between hydrogen peroxide and $^{\bullet}O_2^-$, leading to the generation of $^{\bullet}OH$ through a non-selective process.[65–67] Nevertheless, for LQM PSs, no generation of $^{\bullet}O_2^-$ was detected during photosensitization. This suggests that LQM PSs produce $^{\bullet}OH$ through a mechanism distinct from the Haber–Weiss reaction, but rather *via* a selective photogeneration pathway.

Insight into the H_2O–O_2–$^{\bullet}OH$ oxygen-chain cascade photochemical mechanism

The unique ability of LQM PSs to selectively generate $^{\bullet}OH$ prompted further investigation of their underlying mechanism (Fig. 5a). With this in mind, we then conducted electron spin resonance (ESR) spectroscopy, employing 5,5-dimethyl-1-pyrroline *N*-oxide (DMPO) as a spin-trapping agent. Given that the generation of $^{\bullet}OH$ typically relies on the simultaneous

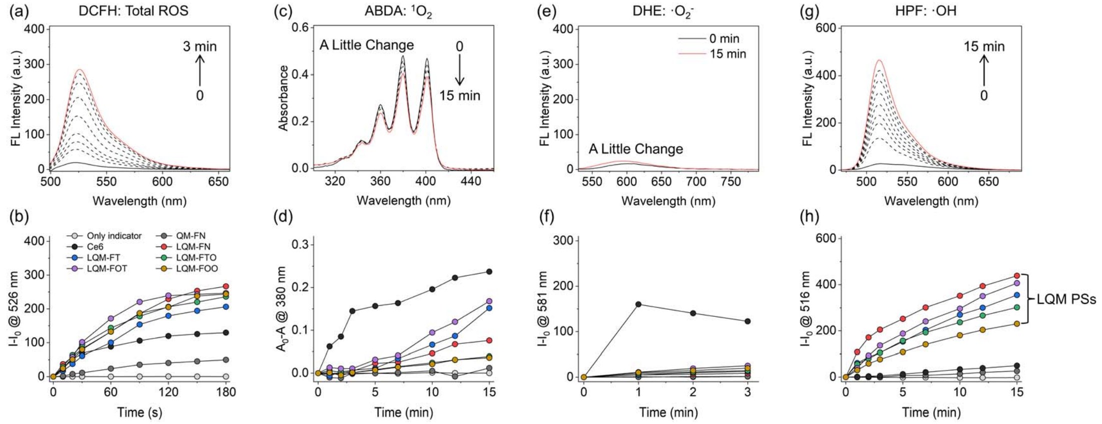

Fig. 4 Selective generation of hydroxyl radicals by LQM PSs. (a, e and g) Fluorescence spectra or (c) absorption spectra of DCFH (a), ABDA (c), DHE (e), and HPF (g) after irradiation (40 μM, 635 nm, 50 mW cm^{-2}, irradiation time of 1 min corresponding to an energy dose of 3 J cm^{-2}) at different times in the presence of LQM-FN (10 μM). (b, f and h) Time-dependent changes in fluorescence intensity or (d) absorbance of DCFH (b, monitored at 526 nm), ABDA (d, monitored at 380 nm), DHE (f, monitored at 581 nm), and HPF (h, monitored at 516 nm) under light irradiation (40 μM, 50 mW cm^{-2}, irradiation time of 1 min corresponding to an energy dose of 3 J cm^{-2}), in the absence or presence of different photosensitizers (10 μM). I_0 is the emission intensity of different indicators (40 μM) before irradiation. A_0 is the absorbance of ABDA (40 μM) before irradiation. Note: the light power density was measured using a power meter at the position of the cuvettes, which were fixed at a distance of 15 cm from the light source.

presence of O_2 and H_2O,[43,68] we carried out ESR analysis under three distinct conditions: (i) in the presence of both H_2O and O_2, (ii) in an anhydrous environment with O_2, and (iii) in an aqueous environment devoid of O_2. In aqueous solution under air, light-activated LQM PSs produced a characteristic 1 : 2 : 2 : 1 quartet ESR signal (Fig. 5b and S9), indicative of $^{\bullet}$OH/DMPO adduct formation. In dichloromethane solution under air, photoactivation yielded signals corresponding to carbon-centered-radical/DMPO adducts and cyano radical/DMPO adducts (Fig. 5c and S10). Notably, even in the absence of O_2 in aqueous solution, LQM PSs still gave rise to $^{\bullet}$OH/DMPO signals, accompanied by spectral features indicative of a mixture of $^{\bullet}$OH, carbon-centered radicals and cyano radicals (Fig. 5d). Taken together, the results under conditions (i) and (ii) indicate that photoactivation of LQM PSs leads to their transformation into radicals while generating $^{\bullet}$OH. And the ESR analysis under condition (iii) implies LQM PSs' capability for photocatalytic H_2O splitting to generate O_2.

Ion chromatography showed that no CN^- was detected in the irradiated aqueous solution of LQM PSs (Fig. S11), indicating that cyano radicals are not generated through covalent bond homolysis and therefore do not transform into cyanide species in the absence of spin-trapping agents such as DMPO. Combined with ESR measurements, the signals corresponding to both cyano radical/DMPO and carbon-centered-radical/DMPO adducts suggest that the spin density of the LQM PS radical is not confined to a single atomic center but is likely delocalized over the π-conjugated framework (Fig. S12). Moreover, these ESR signals gradually decreased and eventually disappeared with increasing O_2 concentration (Fig. S13). Under an O_2 atmosphere, no radical species derived from covalent bond homolysis (including hydrogen and fragment-derived radicals) were detected except for $^{\bullet}$OH (Fig. S14). These results indicate that the LQM PS radical is a delocalized radical species, functioning as a photocatalyst that mediates electron transfer processes.

To thermodynamically validate the H_2O oxidation (for O_2 production) and O_2 reduction (for $^{\bullet}$OH generation) processes observed in ESR, we investigated the redox properties of LQM PSs based on energy band theory (Fig. 5e and S15). The oxidation ability of photogenerated holes and the reduction ability of photogenerated electrons depend on the valence band and conduction band potentials of the photosensitizers, respectively.[48] Representative examples, LQM-FN and LQM-FOO, exhibited valence band potentials of 1.37 V and 1.47 V, respectively, both substantially exceeding the potential of H_2O/O_2, H^+ (0.81 V *vs.* the normal hydrogen electrode, NHE). This provides a strong thermodynamic driving force for photocatalytic O_2 release. Additionally, their conduction band potentials (LQM-FN: −0.10 V; LQM-FOO: 0.01 V) fall between the potential of $O_2/^{\bullet}O_2^-$ (−0.33 V *vs.* NHE) and O_2, $H^+/^{\bullet}OH$ (0.31 V *vs.* NHE), enabling electron transfer to O_2 for selective $^{\bullet}$OH generation. These data provide thermodynamic evidence that corroborates the ROS indicator assays and ESR results, supporting a H_2O–O_2–$^{\bullet}$OH cascade photochemical mechanism.

Interestingly, although QM-FN also fulfills the thermodynamic prerequisites for the oxygen-chain process (Fig. 5e and S16), it neither generated ROS nor displayed detectable ESR signals (Fig. 4 and 5b–d). This highlights the critical role of malononitrile relocation, which extends the conjugation length between the donor and acceptor by four additional carbon atoms. We further performed time-dependent density functional theory (TD-DFT) analysis to elucidate the electron–hole distribution in the T_1 state (Fig. 5l–n and S17). Compared to QM-FN, LQM-FN exhibited reduced overall distribution scale of electrons and holes (3.56 Å *vs.* 4.14 Å), an increased hole delocalization index (7.44 *vs.* 6.41) and an increased electronic delocalization index (6.91 *vs.* 5.74), indicating higher

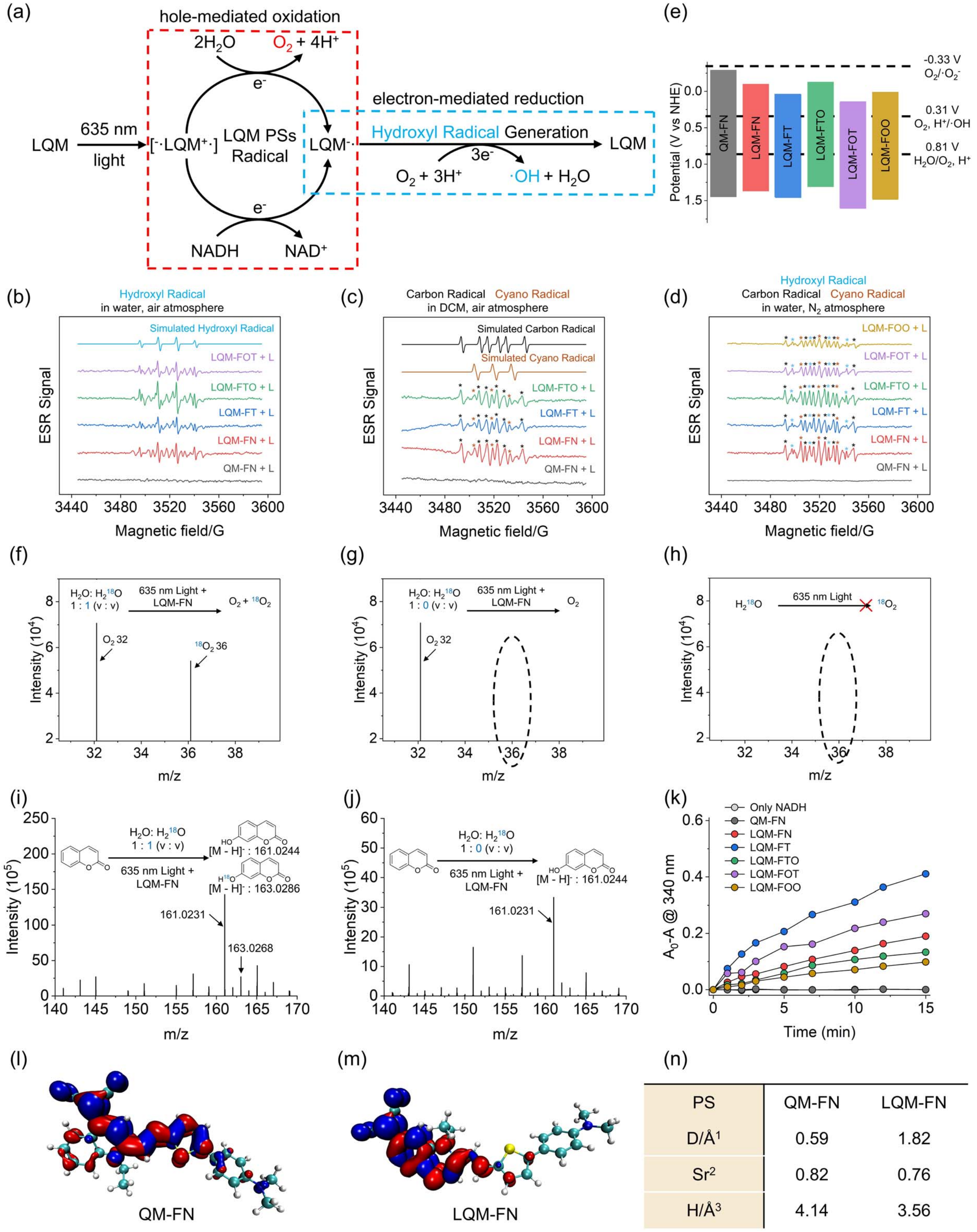

PS	QM-FN	LQM-FN
D/Å[1]	0.59	1.82
Sr[2]	0.82	0.76
H/Å[3]	4.14	3.56

Fig. 5 H_2O–O_2–$^{\bullet}OH$ oxygen-chain cascade photochemical mechanism of LQM PSs. (a) Schematic illustration of the oxygen-chain cascade pathway. Upon photoexcitation, LQM PSs generate a charge-separated state ([$^{-\bullet}$LQM$^{+\bullet}$]). The enhanced charge separation induced by acceptor relocation from QM to LQM facilitates the following processes: (i) hole-mediated oxidation: the photogenerated holes with an oxidation potential > 0.81 V in LQM PSs oxidize H_2O to produce O_2 (or oxidize NADH into NAD^+), while electrons derived from H_2O (or NADH) replenish the holes in LQM PSs, thereby forming the LQM PS radical. (ii) Electron-mediated reduction: the photogenerated electrons with a reduction potential between −0.33 and 0.31 V in the LQM PS radical are transferred to O_2 to generate $^{\bullet}OH$, after which LQM PSs return to the ground state and continuously participate in the photocatalytic cycle under light irradiation. (b) Simulated ESR signals of $^{\bullet}OH$/DMPO adducts and ESR signals of DMPO spin adducts confirming $^{\bullet}OH$ generation by LQM PSs upon irradiation under air in aqueous solution. (c) Simulated ESR signals of carbon-centered radical/DMPO adducts, simulated ESR signals of cyano radical/DMPO adducts, and ESR signals of DMPO spin adducts confirming carbon-centered radicals and cyano radicals generation by LQM PSs upon irradiation in dichloromethane solution under air. Note: the black stars

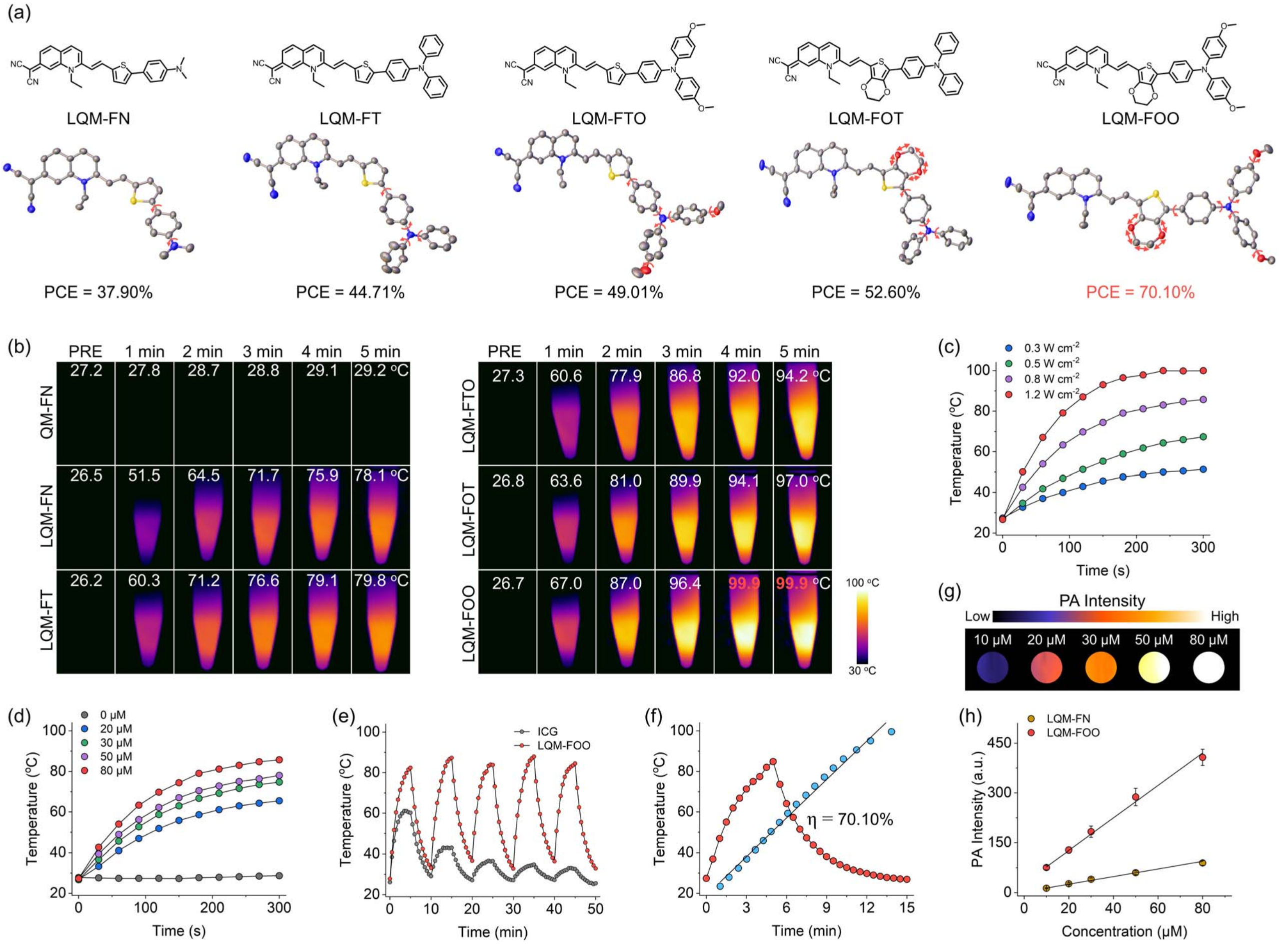

Fig. 6 Photothermal and photoacoustic performance of LQM PSs. (a) Single-crystal X-ray structures of LQM PSs. Note: solvent molecules and H atoms are omitted for clarity. (b) Photothermal images of QM-FN and LQM PSs (80 μM) after irradiation (635 nm, 1.2 W cm^{-2}, irradiation time of 1 min corresponding to an energy dose of 72 J cm^{-2}) at different time points. (c) Photothermal conversion of LQM-FOO (80 μM) under 635 nm light irradiation with different power densities (0.3–1.2 W cm^{-2}, irradiation time of 1 min corresponding to energy doses of 18, 30, 48, and 72 J cm^{-2}, respectively). (d) Photothermal conversion of LQM-FOO at different concentrations (0–80 μM) under 635 nm light irradiation (0.8 W cm^{-2}, irradiation time of 1 min corresponding to an energy dose of 48 J cm^{-2}). (e) Photothermal stability study of LQM-FOO and FDA-approved ICG during five successive "irradiation–cooling" cycles. (f) Photothermal conversion efficiency determination of LQM-FOO. (g) Photoacoustic images of LQM-FOO at different concentrations, $\lambda_{ex} = 660$ nm. (h) Linear relationship between the photoacoustic signal intensity at 660 nm and the concentration of LQM-FOO or LQM-FN. Note: the light power density was measured using a power meter at the position of the centrifuge tubes, which were fixed at a distance of 15 cm from the light source.

localization of electron–hole distribution. Additionally, LQM-FN showed a larger electron–hole centroid distance (1.82 Å *vs.* 0.59 Å) and lower electron–hole overlap (0.76 *vs.* 0.82), reflecting superior electron–hole separation compared to QM-FN. The Chole–Cele function diagram visually underscores the enhanced electron–hole separation in LQM-FN (Fig. S18). These

represent carbon-centered radicals; the brown stars represent cyano radicals. (d) ESR signals of DMPO spin adducts confirming the generation of $^{\bullet}$OH, carbon-centered radicals and cyano radicals by LQM PSs upon irradiation under a nitrogen atmosphere in aqueous solution. Note: the blue stars represent $^{\bullet}$OH, the black stars represent carbon-centered radicals, and the brown stars represent cyano radicals. (e) Energy-level diagram of QM-FN and LQM PSs. (f) Mass spectra of the photocatalytically generated $^{18}O_2$ products using LQM-FN as the photosensitizer in H_2O containing $H_2{}^{18}O$ (v/v = 1 : 1). (g) Mass spectra confirming the absence of photocatalytically generated $^{18}O_2$ products using LQM-FN as the photosensitizer in H_2O lacking $H_2{}^{18}O$ (v/v = 1 : 0). (h) Mass spectra confirming the absence of photocatalytically generated $^{18}O_2$ products in the absence of LQM PSs in $H_2{}^{18}O$. (i) Mass spectra of the products generated from the reaction of $^{\bullet 18}$OH with coumarin using LQM-FN as the photosensitizer in H_2O containing $H_2{}^{18}O$ (v/v = 1 : 1). (j) Mass spectra confirming the absence of products from the reaction of $^{\bullet 18}$OH with coumarin using LQM-FN as the photosensitizer in H_2O lacking $H_2{}^{18}O$ (v/v = 1 : 0). (k) Time-dependent changes in absorbance of NADH (100 μM, monitored at 340 nm) under irradiation (50 mW cm^{-2}, irradiation time of 1 min corresponding to an energy dose of 3 J cm^{-2}), in the absence or presence of different photosensitizers (10 μM). A_0 is the absorbance of NADH (100 μM) before irradiation. (l and m) The distributions of holes (blue) and electrons (red) in the T_1 state of QM-FN (l) and LQM-FN (m). (n) Descriptor obtained from electron–hole analysis. ^{1}Distance between the electron and hole, with an increase in distance correlating with a more distinct charge separation. ^{2}A metric characterizing the overlap between the electron and hole, where a higher value denotes a more substantial overlap, conversely, a lower value implies a more pronounced charge separation. ^{3}A measure of the overall distribution scale of the electron and hole, with a smaller value implying a more focused distribution.

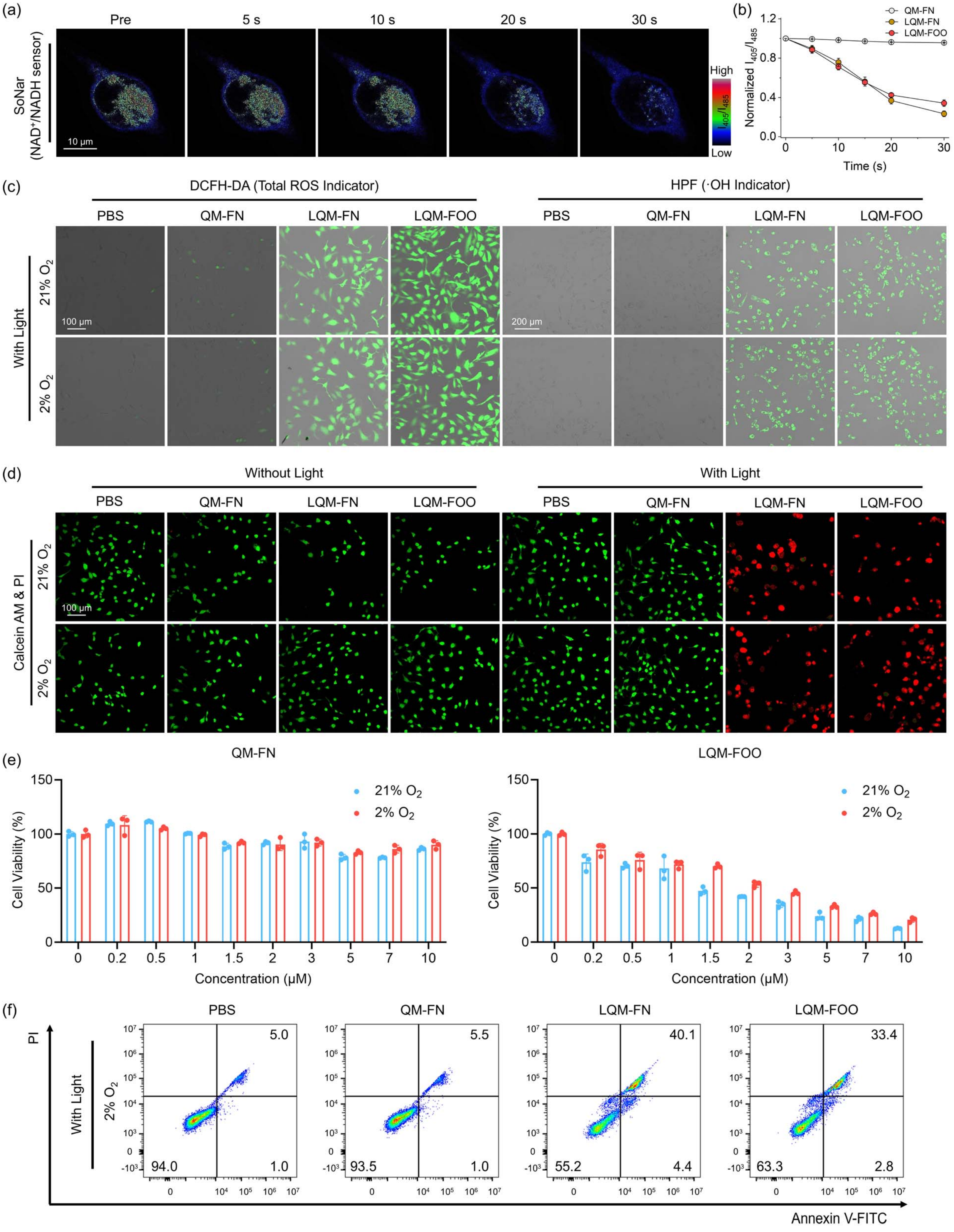

Fig. 7 Oxygen-independent cellular photocytotoxicity. (a) Detection of the NAD$^+$/NADH ratio using SoNar after incubation with LQM-FN (10 μM) upon irradiation (635 nm, 50 mW cm^{-2}, irradiation time of 1 min corresponding to an energy dose of 3 J cm^{-2}) at different time points. Note: a low I_{405}/I_{485} ratio indicates a high NAD$^+$/NADH ratio. (b) Normalized ratio of fluorescence intensities excited at 405 nm and 485 nm after incubation with QM-FN, LQM-FN, or LQM-FOO (10 μM) and irradiation (635 nm, 50 mW cm^{-2}, irradiation time of 1 min corresponding to an energy dose of 3 J cm^{-2}) at different time points. Data are expressed as the mean ± SD of three independent experiments. (c) Detection of intracellular total ROS production (DCFH-DA as the indicator, $\lambda_{ex} = 488$ nm, $\lambda_{em} = 525$–580 nm) or $^{\bullet}$OH production (HPF as the indicator, $\lambda_{ex} = 450$ nm, $\lambda_{em} = 510$–580 nm) after incubation with PBS, QM-FN@FA NPs, LQM-FN@FA NPs, and LQM-FOO@FA NPs (10 μM), with 660 nm light

theoretical insights establish that malononitrile relocation of LQM PSs facilitates long-range ICT to generate an efficient electron–hole separation, promoting the kinetic progression of the H_2O–O_2–$^{\bullet}OH$ cascade pathway.

To further validate the H_2O–O_2–$^{\bullet}OH$ cascade photochemical mechanism, we conducted isotopic mass spectrometric analysis using $H_2{}^{18}O$. First, the photocatalytic generation of O_2 from H_2O was confirmed: upon light irradiation of LQM PSs in H_2O containing $H_2{}^{18}O$, a signal at $m/z = 36$ corresponding to $^{18}O_2$ was observed (Fig. 5f and S19). In contrast, this signal was absent in pure H_2O in the presence of LQM PSs (Fig. 5g and S19), in pure $H_2{}^{18}O$ in the absence of LQM PSs (Fig. 5h), and in H_2O containing $H_2{}^{18}O$ in the presence of LQM PSs but in the absence of light irradiation (Fig. S20). Second, the *in situ* generated O_2 product could be further photosensitively reduced to $^{\bullet}OH$. To confirm this, coumarin was employed in a mixture of H_2O and $H_2{}^{18}O$, yielding a characteristic signal at $m/z = 163.0268$ corresponding to the coumarin–$^{\bullet18}OH$ adduct upon light irradiation in the presence of LQM PSs (Fig. 5i and S19). This signal was absent when only pure H_2O was used under identical conditions (Fig. 5j and S19). These isotopic mass spectrometry results strongly support the H_2O–O_2–$^{\bullet}OH$ oxygen-chain cascade mechanism proposed by thermodynamic and ESR studies. Furthermore, by monitoring the UV-vis absorption spectrum of NADH, a progressive decrease in absorbance at 340 nm and a corresponding increase at 260 nm were observed upon light irradiation in the presence of LQM PSs (Fig. 5k and S21). This suggests that LQM PSs can directly abstract hydrogen atoms from biological substrates, thereby disrupting the redox homeostasis of the microenvironment and enhancing photocatalytic therapy efficacy.

Taken together, we propose a H_2O–O_2–$^{\bullet}OH$ oxygen-chain cascade photogeneration strategy (Fig. 5a). Upon light irradiation, LQM PSs are photoactivated to induce long-range ICT, in which the formation of a charge-separated state can oxidize H_2O to generate O_2. Subsequently, the LQM PS radical transfers electrons to O_2 to produce $^{\bullet}OH$. This novel mechanism, fundamentally distinct from classical PDT pathways, selectively generates the potent $^{\bullet}OH$ species even under O_2-free conditions, potentially offering enhanced phototherapeutic outcomes in hypoxic tumors.

Oxygen-independent synergetic phototherapy in hypoxic cancer cells

Upon light irradiation, a portion of the energy absorbed by photosensitizers is dissipated as heat *via* nonradiative decay.[69,70] Harnessing this thermal energy presents a promising approach to enhance the therapeutic efficacy of phototherapy (Fig. 6). To this end, we evaluated the photothermal conversion capabilities of QM-FN and LQM PSs (Fig. 6b). Under 635 nm light irradiation for 5 minutes, QM-FN induced only a negligible increase in temperature (2 °C, Fig. S22). In contrast, the LQM PSs exhibited pronounced photothermal effects: LQM-FN reached 78.1 °C within 5 minutes, and LQM-FOO rapidly increased to 99.9 °C within just 4 minutes. Further temperature elevation for LQM-FOO was constrained by the boiling point of H_2O. These results highlight that the relocation of malononitrile enables efficient photothermal conversion under red light.

Next, we investigated the photothermal conversion performance of LQM PSs as a function of both light power density and PS concentration. A clear positive correlation was observed between the photothermal effect and these two parameters (Fig. 6c, d and S23). For instance, at a fixed concentration of LQM-FOO (80 μM), increasing the light power density (0.3, 0.5, 0.8, and 1.2 W cm^{-2}, irradiation time of 1 min corresponding to energy doses of 18, 30, 48, and 72 J cm^{-2}, respectively) led to temperature increases to 51.3, 67.3, 85.7, and 99.9 °C, respectively (Fig. 6c). In addition, LQM PSs exhibited excellent photothermal stability, maintaining consistent performance over five successive "irradiation–cooling" cycles (Fig. 6e). This stability far exceeded that of ICG, which exhibited only a 5.4 °C temperature increase in the fifth cycle (Fig. 6e). These findings underscore the outstanding photothermal conversion capabilities of LQM PSs, highlighting their potential for high-performance photothermal therapy.

We further evaluated the photothermal conversion efficiency (PCE) of LQM PSs (Fig. 6f and S23). The calculated PCE values were 37.90% for LQM-FN, 44.71% for LQM-FT, 49.01% for LQM-FTO, 52.60% for LQM-FOT, and as high as 70.10% for LQM-FOO. This enhanced photothermal conversion efficiency originates from the molecular structure containing more rotational and vibrational components, which enable more effective photothermal conversion (Fig. 6a). Furthermore, LQM-FOO exhibited much higher photoacoustic (PA) intensity than LQM-FN (Fig. 6g and h), which was in strong agreement with their PCE values. These results demonstrate LQM PSs as versatile agents not only for high-performance photocatalytic therapy and photothermal therapy, but also for multiplex imaging involving fluorescence imaging, photothermal imaging, and PA imaging.

To impart dual-targeting capabilities of LQM PSs, including active targeting (folic acid, FA-mediated targeting) and passive

irradiation (50 mW cm^{-2} for 5 min, irradiation time of 1 min corresponding to an energy dose of 3 J cm^{-2}), in different O_2 content environments. (d) Calcein acetoxymethyl ester (calcein AM)/propidium iodide (PI) staining of live (green channel, $\lambda_{ex} = 488$ nm, $\lambda_{em} = 500$–530 nm) and dead (red channel, $\lambda_{ex} = 545$ nm, $\lambda_{em} = 590$–640 nm) cells after incubation with PBS, QM-FN@FA NPs, LQM-FN@FA NPs, and LQM-FOO@FA NPs (10 μM), with or without 660 nm light irradiation (50 mW cm^{-2} for 15 min, irradiation time of 1 min corresponding to an energy dose of 3 J cm^{-2}), in different O_2 content environments. (e) Evaluation of cancer cell-killing efficiency by MTT assay after incubation with different concentrations of QM-FN@FA NPs or LQM-FOO@FA NPs, with 660 nm light irradiation (50 mW cm^{-2} for 15 min, irradiation time of 1 min corresponding to an energy dose of 3 J cm^{-2}), in different O_2 content environments. Data are expressed as the mean ± SD of three independent experiments. (f) Apoptosis evaluation by flow cytometry after incubation with PBS, QM-FN@FA NPs, LQM-FN@FA NPs, or LQM-FOO@FA NPs (1 μM), with 660 nm light irradiation (50 mW cm^{-2} for 15 min, irradiation time of 1 min corresponding to an energy dose of 3 J cm^{-2}), in a 2% O_2 content environment. Note: the light power density was measured using a power meter at the position of the cell culture dishes, which were fixed at a distance of 5 cm from the light source.

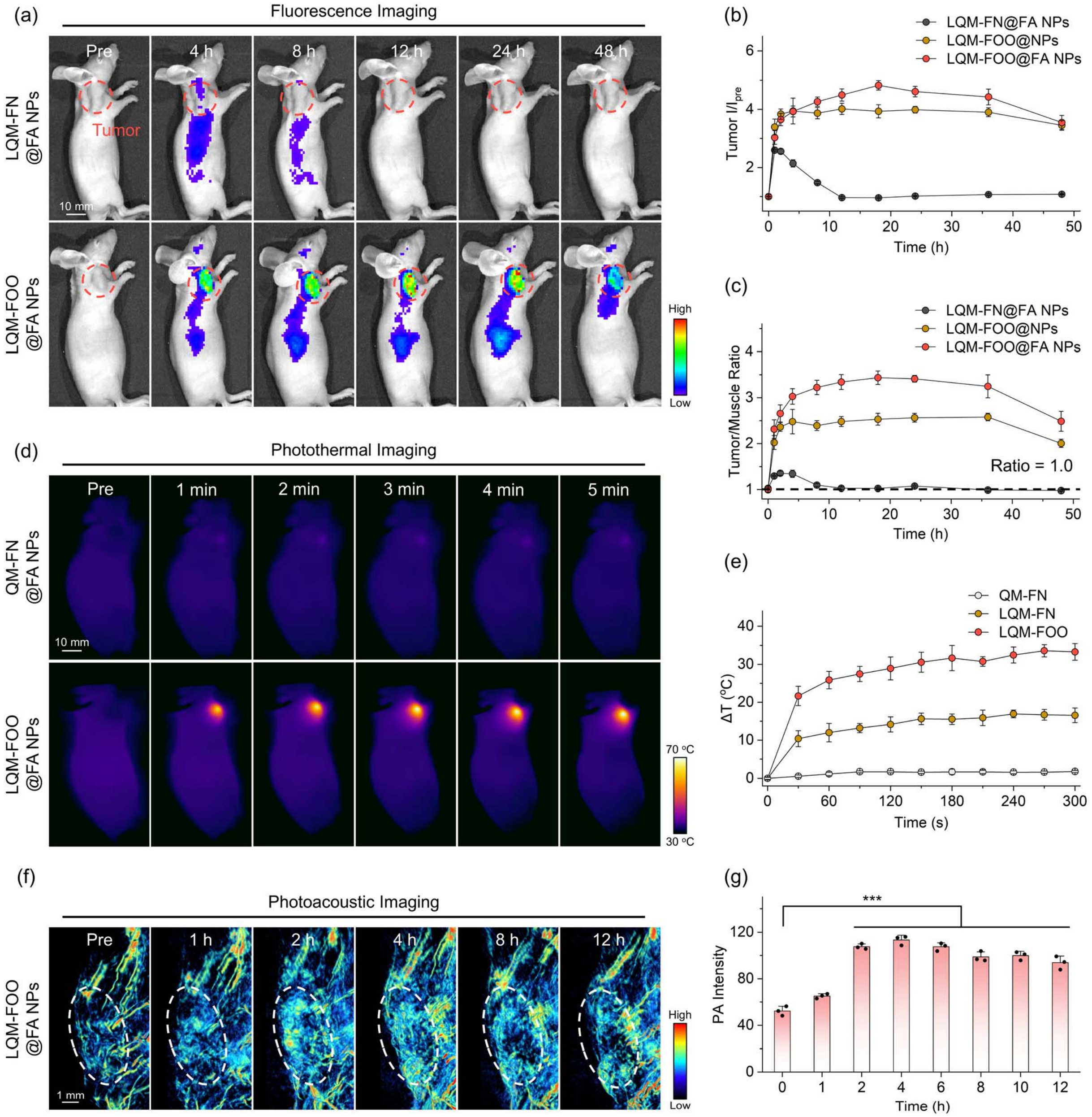

Fig. 8 Multiplex imaging in tumor-bearing mice. (a) *In vivo* fluorescence imaging of SKOV3 xenograft tumor-bearing mice at different time points following intravenous administration of LQM-FN@FA NPs or LQM-FOO@FA NPs (0.5 mg mL^{-1}, 200 μL, $\lambda_{ex} = 600 \pm 10$ nm, $\lambda_{em} = 845 \pm 20$ nm). (b) Tumor relative fluorescent intensity profiles following intravenous administration of LQM-FN@FA NPs, LQM-FOO@NPs, or LQM-FOO@FA NPs. Data are expressed as the mean ± SD of three independent mice. (c) Tumor-to-muscle fluorescent intensity ratios of LQM-FN@FA NPs, LQM-FOO@NPs, and LQM-FOO@FA NPs over 48 hours post-injection. Data are expressed as the mean ± SD of three independent mice. (d) *In vivo* photothermal imaging of SKOV3 xenograft tumor-bearing mice at different time points following administration of QM-FN@FA NPs or LQM-FOO@FA NPs (under irradiation at 635 nm, 0.2 W cm^{-2}, irradiation time of 1 min corresponding to an energy dose of 12 J cm^{-2}). Note: the light power density was measured using a power meter at the position of the mice, which were fixed at a distance of 15 cm from the light source. (e) Temperature changes profiles following administration of QM-FN@FA NPs, LQM-FN@FA NPs, and LQM-FOO@FA NPs. Data are expressed as the mean ± SD of three independent mice. (f) *In vivo* photoacoustic imaging of SKOV3 xenograft tumor-bearing mice at different time points following intravenous administration of LQM-FOO@FA NPs ($\lambda_{ex} = 660$ nm). (g) Tumor photoacoustic intensity profiles extracted from the imaging results shown in panel (f). Data are expressed as the mean ± SD of three independent mice. Statistical significance (P value) is calculated by a two-sided t-test. ***$P < 0.001$.

targeting (enhanced permeability and retention effect),[71–73] LQM PSs were encapsulated using FA-modified or unmodified amphiphilic polymers (DSPE–PEG2000–FA and DSPE–PEG2000). Confocal laser scanning microscopy (CLSM) and flow cytometry revealed negligible differences in uptake between the two nanoparticles in normal cells (human renal tubular epithelial cell line Hk2, Fig. S24 and S25). In contrast, in the human ovarian cancer cell line SKOV3, the uptake efficiency of

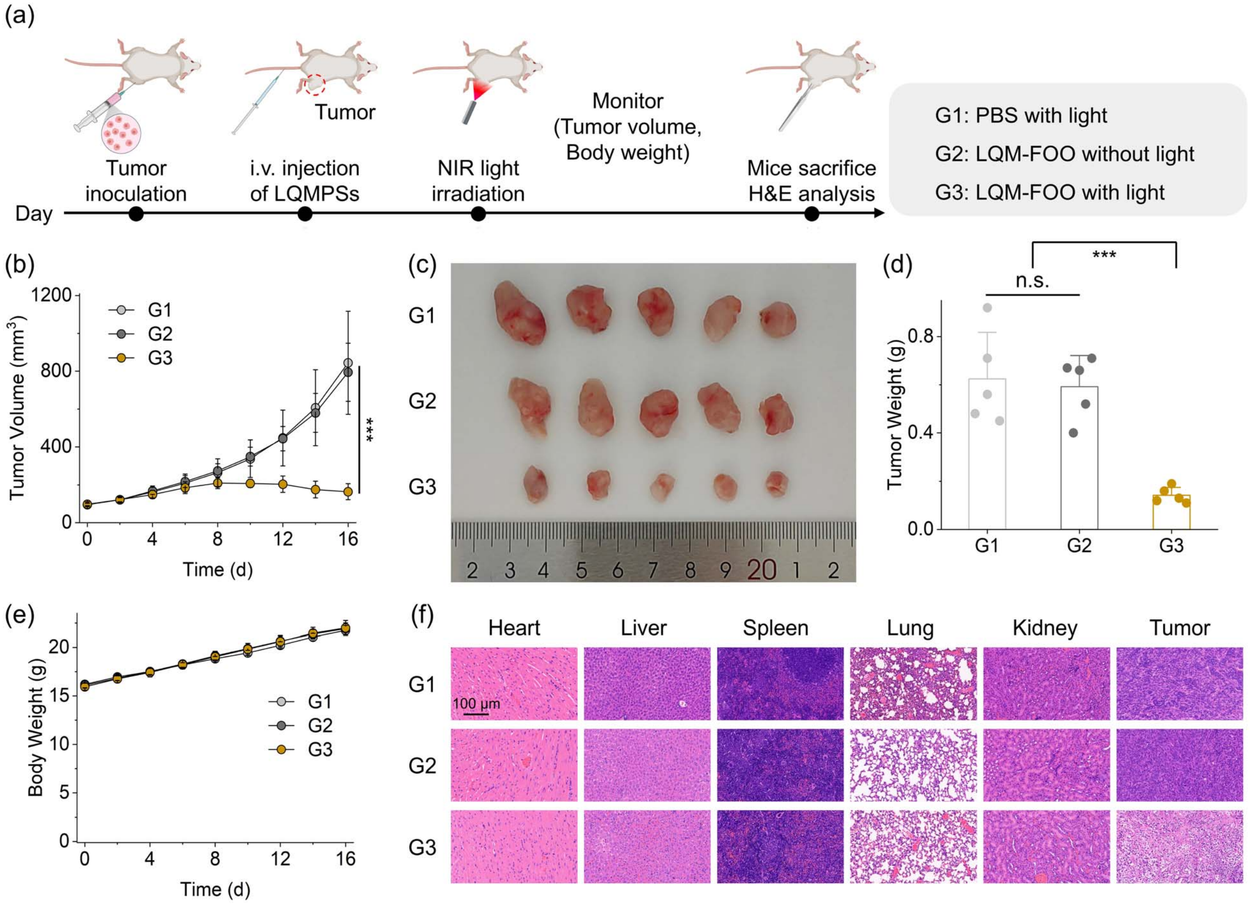

Fig. 9 *In vivo* phototherapy against SKOV3 tumor. (a) Schematic representation of the therapy timeline for *in vivo* antitumor efficacy of LQM PSs. (b) Tumor volumes of SKOV3 tumor-bearing mice after intravenous injection with PBS or LQM-FOO@FA NPs (0.5 mg mL^{-1}, 200 μL), without or with 635 nm light irradiation (0.2 W cm^{-2}, 20 min, irradiation time of 1 min corresponding to an energy dose of 12 J cm^{-2}). Data are expressed as the mean ± SD of $n = 5$ mice. Note: the light power density was measured using a power meter at the position of the mice, which were fixed at a distance of 15 cm from the light source. (c) Tumor photographs and (d) tumor weights of SKOV3 tumor-bearing mice after different treatments. Data are expressed as the mean ± SD of $n = 5$ mice. (e) Body weights of SKOV3 tumor-bearing mice during the treatment period. Data are expressed as the mean ± SD of $n = 5$ mice. (f) H&E staining of various organ sections from mice after different treatments. Statistical significance (P value) is calculated by a two-sided t-test. n.s.: not significant, ***$P < 0.001$.

LQM PSs encapsulated with DSPE–PEG2000–FA was significantly higher than that of those encapsulated with DSPE–PEG2000 (Fig. S24 and S25). These results indicate the key role of FA-functionalized encapsulation in facilitating the selective accumulation of LQM PSs in tumor cells, offering a promising approach for tumor-specific theranostic applications.

To evaluate the therapeutic efficacy of LQM PSs, we selected LQM-FN and LQM-FOO (encapsulation with DSPE–PEG2000–FA) as representative candidates due to their superior $^{\bullet}$OH generation and photothermal capabilities, alongside QM-FN as a control. We employed SoNar, a genetically encoded fluorescent sensor,[74] to assess the capacity of LQM PSs to catalyze the oxidation of NADH to NAD$^+$ in living cells. The SoNar fluorescence intensity ratio (I_{405}/I_{485}) decreases upon NADH oxidation, indicating redox perturbation. Light irradiation of QM-FN-treated cells showed no appreciable change in the I_{405}/I_{485} ratio. In contrast, cells treated with LQM-FN or LQM-FOO exhibited a rapid and sustained decrease in the I_{405}/I_{485} ratio following irradiation (Fig. 7a, b and S26). These results confirm the ability of LQM PSs to photocatalytically oxidize intracellular NADH to NAD$^+$, thereby perturbing the redox homeostasis within cancer cells.

Then, we evaluated the intracellular ROS generation capabilities of the LQM PSs using DCFH-DA as a total ROS indicator. As shown in Fig. 7c, S27 and S28, cells incubated with LQM-FN or LQM-FOO exhibited a pronounced fluorescence increase upon irradiation, indicative of efficient ROS-mediated oxidation of DCFH-DA to DCF. Next, we employed HPF as a selective $^{\bullet}$OH indicator. Upon light irradiation, significant fluorescence enhancement was observed in the LQM-FN and LQM-FOO groups, confirming $^{\bullet}$OH production (Fig. 7c, S29 and S30). Importantly, comparable levels of ROS and $^{\bullet}$OH generation were observed under both normoxic and hypoxic (2% O_2 and <0.5% O_2) conditions (Fig. 7c and S27–S31). These results highlight the O_2-independent $^{\bullet}$OH-generating capability of LQM PSs, demonstrating their therapeutic potential within the hypoxic tumor.

The cancer cell-killing performance of LQM PSs was subsequently investigated. Calcein AM/PI dual staining was employed to distinguish live and dead cells. In the absence of light irradiation, negligible cell death was observed across all groups. Upon light irradiation, both LQM-FN and LQM-FOO induced pronounced cell death under both normoxic and hypoxic conditions (Fig. 7d). Concentration-dependent cytotoxicity of LQM PSs was assessed using the MTT assay (Fig. 7e, S32 and S33). While QM-FN exhibited negligible phototoxicity, LQM PSs demonstrated minimal dark toxicity but markedly enhanced cytotoxicity upon light irradiation in a concentration-dependent manner. Specifically, under normoxic conditions, light-irradiated cell viability was 13.4% and 13.0% for LQM-FN and LQM-FOO at 10 μM, with corresponding half maximal inhibitory concentration (IC_{50}) values of 1.06 μM and 1.18 μM, respectively, indicating exceptionally high phototoxic indexes (>433) for both photosensitizers (Fig. S34 and S35). Notably, LQM PSs retained robust cancer cell killing efficacy even under hypoxic conditions, where their IC_{50} values were determined to be 1.61 μM and 2.42 μM, respectively. Furthermore, both LQM-FN and LQM-FOO significantly induced apoptosis under light irradiation, as evidenced by the increased percentage of annexin V/PI double-positive cells detected *via* flow cytometry under both normoxic and hypoxic conditions (Fig. 7f and S36). These findings collectively demonstrate that LQM PSs effectively induce tumor cell death *via* $^{\bullet}$OH-specific phototherapy, highlighting their potential for overcoming the challenges of solid tumors' O_2-deficient conditions.

In vivo multiplex imaging and phototherapy

Leveraging the multiplex imaging capabilities of LQM PSs, LQM-FN and LQM-FOO were intravenously administered into tumor-bearing mice. Fluorescence imaging results demonstrated that LQM-FN@FA NPs exhibited only limited tumor accumulation and underwent rapid clearance from the body (Fig. 8a–c, S37 and S38). This behavior is likely attributable to the tighter molecular stacking of LQM-FN, which resulted in the formation of significantly larger nanoparticles with an average size of approximately 405 nm (Fig. S39 and S40). In contrast, LQM-FOO@FA NPs with an appropriate particle size (112 nm) exhibited a gradually increasing fluorescence signal at the tumor site, peaking at 18 hours and remaining clearly visible even 48 hours post-injection (Fig. 8a, b and S37). Quantitative analysis of tumor-to-muscle fluorescence intensity ratios showed that LQM-FOO@FA NPs achieved a peak ratio (3.4) at 18 hours and maintained it through 36 hours (Fig. 8c). Notably, LQM-FOO@NPs and LQM-FOO@FA NPs exhibited similar particle sizes (Fig. S39 and S40), yet LQM-FOO@FA NPs demonstrated substantially enhanced tumor-targeting capability compared with LQM-FOO@NPs (Fig. 8b, c and S41). This result highlights the critical role of FA in enhancing tumor targeting. *Ex vivo* fluorescence analysis of major organs at 12 hours post-injection confirmed the *in vivo* imaging results (Fig. S38, S41 and S42). Mice treated with LQM-FOO@FA NPs yielded markedly enhanced fluorescence signals in tumor tissue relative to muscle. These fluorescence imaging results confirm that LQM-FOO@FA NPs could accumulate and light-up tumor in living mice.

Next, we evaluated the *in vivo* photothermal and PA imaging performance of the LQM PSs. Upon 5 minutes of 635 nm light irradiation at the tumor site, QM-FN induced a negligible temperature increase ($\Delta T = 1.8$ °C, Fig. 8d and e). In contrast, both LQM-FN and LQM-FOO exhibited sustained temperature elevations, with ΔT values of 16.6 °C and 33.3 °C, respectively (Fig. 8d, e and S43), consistent with their PCE values. Furthermore, LQM-FOO was intravenously administered into tumor-bearing mice, and PA imaging results showed a significant signal enhancement at the tumor site, with sustained accumulation over a prolonged period (Fig. 8f and g). These *in vivo* imaging results demonstrate that LQM PSs effectively integrate fluorescence, photothermal, and PA imaging modalities, offering a robust platform for real-time diagnosis and treatment monitoring.

The tumor-targeting capability and potent cancer cell-killing activity of LQM PSs motivated us to further assess their *in vivo* antitumor efficacy in SKOV3 tumor-bearing mice. Mice were randomly divided into three groups according to the treatment workflow illustrated in Fig. 9a: (G1) PBS with light; (G2) LQM-FOO without light; and (G3) LQM-FOO with light. When tumor volumes reached approximately 100 mm^3 at day 7 post-inoculation, mice received intravenous injections of either PBS or LQM-FOO@FA NPs *via* the tail vein. At 48 h post-injection, tumors in G1 and G3 were irradiated with a 635 nm light (0.2 W cm^{-2}, 20 min, irradiation time of 1 min corresponding to an energy dose of 12 J cm^{-2}). Under these irradiation conditions, the photothermal effect was negligible (Fig. S44), allowing us to specifically evaluate the therapeutic efficacy of oxygen-chain photocatalytic therapy. Tumor progression in all groups was subsequently monitored every two days.

Remarkably, tumor growth in G3 was significantly inhibited relative to that in G1 and G2 (Fig. 9b–d). After 16 days of treatment, major organs (heart, liver, spleen, lung, and kidney) were harvested for hematoxylin and eosin (H&E) staining, which showed no discernible pathological abnormalities (Fig. 9f). In addition, the body weight of all mice steadily increased throughout the study (Fig. 9e), confirming the favorable biosafety profile of LQM PSs *in vivo*. Importantly, histological analysis of tumors from G3 revealed extensive cellular destruction and significant suppression of tumor proliferation (Fig. 9f). Collectively, these findings provide compelling evidence for both the biosafety of LQM PSs and therapeutic efficacy of the H_2O–O_2–$^{\bullet}$OH oxygen-chain cascade photogeneration strategy in tumor treatment. Their ability to integrate multiplex imaging with O_2-independent *in situ* $^{\bullet}$OH-specific phototherapy establishes LQM PSs as promising candidates for advanced theranostic applications.

Conclusions

This work presents a novel LQM scaffold core that allows O_2-independent *in situ* $^{\bullet}$OH-specific photogeneration from H_2O in biological tissues. The chemical innovation in the LQM core—acceptor relocation with long-range ICT—has successfully resolved the long-standing PDT challenge of the therapeutic efficiency and hypoxic limitation. This major breakthrough for photocatalytic therapy is enabled by an unprecedented H_2O–O_2–$^{\bullet}OH$ oxygen-chain cascade photochemical pathway and realizes the evolution of H_2O into $^{\bullet}OH$ *via* a consecutive oxidation and electron transfer process, which cannot be achieved through the classical Haber–Weiss pathway.

Through single-crystal analysis, electron spin resonance spectroscopy, electrochemical characterization, isotopic mass spectrometry, and theoretical calculations, we demonstrated that the acceptor relocation within LQM could orchestrate the oxygen-chain photochemical pathway both in thermodynamic and kinetic perspectives: (i) the finely regulated oxidation/reduction potentials of LQM PSs thermodynamically favor the activation of the H_2O–O_2–$^{\bullet}OH$ oxygen-chain pathway, theoretically allowing $^{\bullet}OH$-specific photogeneration independent of ambient O_2. (ii) LQM PSs exhibit markedly long-range ICT, promoting more effective electron–hole separation (1.82 Å) and thereby accelerating the kinetic progression. We have expanded this molecular engineering method to other D–π–A featured dyes that span the visible, NIR-I, and NIR-II range with oxygen-chain properties, demonstrating the generalizability of our platform. Notably, LQM PSs exhibit robust O_2-independent photocytotoxicity at the cellular level, excellent tumor suppression efficacy and biosafety *in vivo*, underscoring their translational potential. Beyond its practical utility, this design paradigm opens new avenues beyond traditional donor–acceptor strength modulation strategies of organic fluorophores. Taken together, our study highlights how innovative molecular design can overcome longstanding limitations in phototherapy, laying the groundwork for advanced therapeutic strategies that promise greater efficacy, safety, and personalization in future clinical practice.

Ethics approval

All applicable institutional and governmental regulations concerning the ethical use of animals were followed. All animal care and experimental procedures were reviewed and approved by the East China University of Science and Technology Animal Studies Committee (ECUST-2023-026).

Author contributions

All the experiments were conducted by Q. L., X. L., H. H., Z. F., J. Z., W. Z., P. S. and Y. Z. with the supervision of C. Y., W.-H. Z. and Z. G. All the authors analysed the data and contributed to the paper writing.

Conflicts of interest

There are no conflicts to declare.

Data availability

CCDC 2482027 and 2482032–2482036 contain the supplementary crystallographic data for this paper.[75a–f]

The main data supporting the results in this study are available within the paper and its supplementary information (SI). All data generated and analysed during the study are available from the corresponding authors upon reasonable request. Supplementary information: experimental details, characterization data, and supplementary figures. See DOI: https://doi.org/10.1039/d6sc03309a.

Acknowledgements

This work was supported by the National Key Research and Development Program (2023YFA1802000), NSFC/China (22225805, 32121005, 32394001, T2522013, and 22378122), Shanghai Science and Technology Innovation Action Plan (No. 23J21901600), Shanghai Frontier Science Research Base of Optogenetic Techniques for Cell Metabolism (Shanghai Municipal Education Commission, grant 2021 Sci & Tech 03-28), and Science and Technology Commission of Shanghai Municipality (grant No. 24DX1400200).

Notes and references

1 M. P. Murphy, H. Bayir, V. Belousov, C. J. Chang, K. J. A. Davies, M. J. Davies, T. P. Dick, T. Finkel, H. J. Forman, Y. Janssen-Heininger, D. Gems, V. E. Kagan, B. Kalyanaraman, N. G. Larsson, G. L. Milne, T. Nyström, H. E. Poulsen, R. Radi, H. Van Remmen, P. T. Schumacker, P. J. Thornalley, S. Toyokuni, C. C. Winterbourn, H. Yin and B. Halliwell, *Nat. Metab.*, 2022, **4**, 651–662.

2 H. J. Forman and H. Zhang, *Nat. Rev. Drug Discovery*, 2021, **20**, 689–709.

3 M. Lin, X. Lv, H. Wang, L. Shu, H. Wang, G. Zhang, J. Sun and X. Chen, *Adv. Mater.*, 2024, **36**, 2407378.

4 B. Halliwell, A. Adhikary, M. Dingfelderc and M. Dizdaroglu, *Chem. Soc. Rev.*, 2021, **50**, 8355–8360.

5 J. J. Koskimäki, M. Kajula, J. Hokkanen, E. L. Ihantola, J. H. Kim, H. Hautajärvi, E. Hankala, M. Suokas, J. Pohjanen, O. Podolich, N. Kozyrovska, A. Turpeinen, M. Pääkkönen, S. Mattila, B. C. Campbell and A. M. Pirttilä, *Nat. Chem. Biol.*, 2016, **12**, 332–338.

6 S. Mu, H. Lu, Q. Wu, L. Li, R. Zhao, C. Long and C. Cui, *Nat. Commun.*, 2022, **13**, 3694.

7 L. Wu, Y. Ishigaki, W. Zeng, T. Harimoto, B. Yin, Y. Chen, S. Liao, Y. Liu, Y. Sun, X. Zhang, Y. Liu, Y. Liang, P. Sun, T. Suzuki, G. Song, Q. Fan and D. Ye, *Nat. Commun.*, 2021, **12**, 6145.

8 X. Li, J. F. Lovell, J. Yoon and X. Chen, *Nat. Rev. Clin. Oncol.*, 2020, **17**, 657–674.

9 X. Li, X. Ou, Z. Yang, M. Kang, W. Xu, D. Li, R. T. K. Kwok, J. W. Y. Lam, Z. Zhang, D. Wang and B. Z. Tang, *Adv. Mater.*, 2025, **37**, 2416590.

10 L. Jiang, H. Bai, L. Liu, F. Lv, X. Ren and S. Wang, *Angew. Chem., Int. Ed.*, 2019, **58**, 10660–10665.

11 R. Zhang, D. K. Ji, D. Yao, Z. Xiao and W. Tan, *CCS Chem.*, 2024, **6**, 1240–1254.

12 D. Abad-Montero, A. Gandioso, E. Izquierdo-García, S. Chumillas, A. Rovira, M. Bosch, M. Jordà-Redondo,

D. Castaño, J. Bonelli, V. V. Novikov, A. Deyà, J. L. Hernández, J. Galino, M. E. Alberto, A. Francés-Monerris, S. Nonell, G. Gasser and V. Marchán, *J. Am. Chem. Soc.*, 2025, **147**, 7360–7376.

13 X. Liu, W. Zhan, G. Gao, Q. Jiang, X. Zhang, H. Zhang, X. Sun, W. Han, F. G. Wu and G. Liang, *J. Am. Chem. Soc.*, 2023, **145**, 7918–7930.

14 S. Fu, B. Huang, H. Wen, Z. Chen, L. Li, Y. He, L. Fang, Y. Lin and X. Li, *Adv. Mater.*, 2026, **38**, 09641.

15 L. Hou, X. Zhang, T. C. Pijper, W. R. Browne and B. L. Feringa, *J. Am. Chem. Soc.*, 2014, **136**, 910–913.

16 Y. Jiang, J. Huang, X. Zhen, Z. Zeng, J. Li, C. Xie, Q. Miao, J. Chen, P. Chen and K. Pu, *Nat. Commun.*, 2019, **10**, 2064.

17 Y. Qin, L. J. Chen, F. Dong, S. T. Jiang, G. Q. Yin, X. Li, Y. Tian and H. B. Yang, *J. Am. Chem. Soc.*, 2019, **141**, 8943–8950.

18 M. Chiba, M. Kamiya, K. Tsuda-Sakurai, Y. Fujisawa, H. Kosakamoto, R. Kojima, M. Miura and Y. Urano, *ACS Cent. Sci.*, 2019, **5**, 1676–1681.

19 K. Zhou, L. Du, R. Ding, L. Xu, S. Shi, S. Wang, Z. Wang, G. Zhang, G. He, Z. Zhao and B. Z. Tang, *Nat. Commun.*, 2024, **15**, 10551.

20 Q. Yao, J. Fan, S. Long, X. Zhao, H. Li, J. Du, K. Shao and X. Peng, *Chem*, 2022, **8**, 197–209.

21 N. Kwon, H. Weng, M. A. Rajora and G. Zheng, *Angew. Chem., Int. Ed.*, 2025, **64**, 202423348.

22 Z. Yi, X. Qin, L. Zhang, H. Chen, T. Song, Z. Luo, T. Wang, J. Lau, Y. Wu, T. B. Toh, C. S. Lee, W. Bu and X. Liu, *J. Am. Chem. Soc.*, 2024, **146**, 9413–9421.

23 L. Yu, Y. Xu, Z. Pu, H. Kang, M. Li, J. L. Sessler and J. S. Kim, *J. Am. Chem. Soc.*, 2022, **144**, 11326–11337.

24 R. Zhang, H. Xu, Y. Yao, G. Ran, W. Zhang, J. Zhang, J. L. Sessler, S. Gao and J. L. Zhang, *J. Am. Chem. Soc.*, 2023, **145**, 23257–23274.

25 F. Heinemann, J. Karges and G. Gasser, *Acc. Chem. Res.*, 2017, **50**, 2727–2736.

26 P. George, *Nature*, 1947, **159**, 41–43.

27 B. Yang, H. Yao, J. Yang, C. Chen, Y. Guo, H. Fu and J. Shi, *J. Am. Chem. Soc.*, 2022, **144**, 314–330.

28 G. A. Coppola, S. Pillitteri, E. V. Van der Eycken, S. L. You and U. K. Sharma, *Chem. Soc. Rev.*, 2022, **51**, 2313–2382.

29 K. Wei, Y. Wu, X. Zheng, L. Ouyang, G. Ma, C. Ji and M. Yin, *Angew. Chem., Int. Ed.*, 2024, **63**, 202404395.

30 T. C. Pham, V. N. Nguyen, Y. Choi, S. Lee and J. Yoon, *Chem. Rev.*, 2021, **121**, 13454–13619.

31 B. L. Song, J. Q. Wang, G. X. Zhang, N. B. Yi, Y. J. Zhang, L. Zhou, Y. H. Guan, X. H. Zhang, W. F. Zheng, Z. Y. Qiao and H. Wang, *Angew. Chem., Int. Ed.*, 2024, **63**, 202411725.

32 H. Zhao, S. Jin, Y. Liu, Q. Wang, B. S. N. Tan, S. Wang, W. K. Han, X. Niu and Y. Zhao, *J. Am. Chem. Soc.*, 2025, **147**, 4871–4885.

33 L. Ge, Y. Tang, C. Wang, J. Chen, H. Mao and X. Jiang, *Nat. Commun.*, 2024, **15**, 153.

34 H. Zhang, X. Xu, Y. Cao, Z. Chen, W. Liu, X. Lu and C. Li, *Angew. Chem., Int. Ed.*, 2025, **64**, 202424830.

35 D. E. Dolmans, D. Fukumura and R. K. Jain, *Nat. Rev. Cancer*, 2003, **3**, 380–387.

36 P. Chen, J. Rong, K. Chen, T. Huang, Q. Shen, P. Sun, W. Tang and Q. Fan, *Angew. Chem., Int. Ed.*, 2025, **64**, 202418081.

37 M. Brändlin, B. Pfund and O. S. Wenger, *Nat. Chem.*, 2025, **17**, 1777–1784.

38 Y. Kim, J. G. Smith and P. K. Jain, *Nat. Chem.*, 2018, **10**, 763–769.

39 Y. Zheng, T. Zhang, M. Chang, L. Xia, L. Chen, L. Ding, Y. Chen and R. Wu, *Adv. Mater.*, 2025, **37**, 2413601.

40 L. Liu, M. Y. Gao, H. Yang, X. Wang, X. Li and A. I. Cooper, *J. Am. Chem. Soc.*, 2021, **143**, 19287–19293.

41 T. Banerjee, F. Podjaski, J. Kröger, B. P. Biswal and B. V. Lotsch, *Nat. Rev. Mater.*, 2020, **6**, 168–190.

42 P. He, M. Jia, L. Yang, H. Zhang, R. Chen, W. Yao, Y. Pan, Q. Fan, W. Hu and W. Huang, *Adv. Mater.*, 2025, **37**, 2418978.

43 S. Yao, F. Xu, Y. Wang, J. Shang, S. Li, X. Xu, Z. Liu, W. He, Z. Guo and Y. Chen, *J. Am. Chem. Soc.*, 2025, **147**, 11132–11144.

44 J. Liu, Z. Zhao, C. Deng, R. Zanni, R. R. Weichselbaum and W. Lin, *J. Am. Chem. Soc.*, 2025, **147**, 25622–25634.

45 D. Shi, W. Liu, Y. Gao, X. Li, Y. Huang, X. Li, T. D. James, Y. Guo and J. Li, *Nat. Aging*, 2023, **3**, 297–312.

46 C. Wang, Q. Qiao, W. Chi, J. Chen, W. Liu, D. Tan, S. McKechnie, D. Lyu, X. F. Jiang, W. Zhou, N. Xu, Q. Zhang, Z. Xu and X. Liu, *Angew. Chem., Int. Ed.*, 2020, **59**, 10160–10172.

47 Q. Liu, C. Sun, R. Dai, C. Yan, Y. Zhang, W. H. Zhu and Z. Guo, *Coord. Chem. Rev.*, 2024, **503**, 215652.

48 K. X. Teng, L. Y. Niu and Q. Z. Yang, *J. Am. Chem. Soc.*, 2023, **145**, 4081–4087.

49 L. Chen, S. Yan, W. J. Guo, L. Qiao, X. Zhan, B. Liu and H. Q. Peng, *Chem. Sci.*, 2024, **15**, 16059–16068.

50 X. Li, Y. Tan, Z. Li, Y. Wang, C. Lu, S. Liao, B. Yin, B. Chen, H. Liu, H. Wei and G. Song, *J. Am. Chem. Soc.*, 2025, **147**, 26518–26533.

51 X. Yang, G. I. N. Waterhouse, S. Lu and J. Yu, *Chem. Soc. Rev.*, 2023, **52**, 8005–8058.

52 J. Dai, W. Wei, C. Yan, D. K. Ji, C. Liu, J. Huang, C. Liang, J. Liu, Z. Guo and W. H. Zhu, *Nat. Biomed. Eng.*, 2025, **9**, 1632–1644.

53 C. Shi, Z. Guo, Y. Yan, S. Zhu, Y. Xie, Y. S. Zhao, W. H. Zhu and H. Tian, *ACS Appl. Mater. Interfaces*, 2013, **5**, 192–198.

54 N. Ruan, Q. Qiu, X. Wei, J. Liu, L. Wu, N. Jia, C. Huang and T. D. James, *J. Am. Chem. Soc.*, 2024, **146**, 2072–2079.

55 Z. Guo, C. Yan and W. H. Zhu, *Angew. Chem., Int. Ed.*, 2020, **59**, 9812–9825.

56 K. An, Q. Qiao, L. Vashist, S. A. A. Abedi, X. Liu and Z. Xu, *Chin. Chem. Lett.*, 2025, **36**, 109786.

57 L. Zhang, W. Wang, Y. Q. Zhao, R. Huang, Y. Lu, Y. Chen, L. Duan and Y. Zhou, *Chin. Chem. Lett.*, 2025, **36**, 109798.

58 L. Zhang, S. C. Wan, J. Zhang, M. J. Zhang, Q. C. Yang, B. Zhang, W. Y. Wang, J. Sun, R. T. K. Kwok, J. W. Y. Lam, H. Deng, Z. J. Sun and B. Z. Tang, *J. Am. Chem. Soc.*, 2023, **145**, 17689–17699.

59 C. R. Benson, L. Kacenauskaite, K. L. VanDenburgh, W. Zhao, B. Qiao, T. Sadhukhan, M. Pink, J. Chen, S. Borgi, C. H. Chen, B. J. Davis, Y. C. Simon,

K. Raghavachari, B. W. Laursen and A. H. Flood, *Chem*, 2020, **6**, 1978–1997.

60 H. Zhu, Q. Li, B. Shi, F. Ge, Y. Liu, Z. Mao, H. Zhu, S. Wang, G. Yu, F. Huang and P. J. Stang, *Angew. Chem., Int. Ed.*, 2020, **59**, 20208–20214.

61 Y. Lei, Y. Wang, S. K. Hill, Z. Cheng, Q. Song and S. Perrier, *Adv. Mater.*, 2024, **36**, 2401346.

62 W. Zhou, Y. C. Liu, G. J. Liu, Y. Zhang, G. L. Feng and G. W. Xing, *Angew. Chem., Int. Ed.*, 2025, **64**, 202413350.

63 Y. Yu, L. Zhang, H. Jia, C. Ji, Y. Liu, Z. Zhao, C. Dai, D. Ding, B. Z. Tang and G. Feng, *ACS Nano*, 2024, **18**, 31286–31299.

64 J. Tian, B. Li, C. Wu, Z. Li, W. Song, B. Song, Y. Tang, W. Pan and B. Liu, *J. Am. Chem. Soc.*, 2025, **147**, 31310–31323.

65 W. H. Koppenol, *Redox Rep.*, 2001, **6**, 229–234.

66 W. G. Barb, J. H. Baxendale, P. George and K. R. Hargrave, *Nature*, 1949, **163**, 692–694.

67 X. Li, L. Huang, G. Baryshnikov, A. Ali, P. Dai, Z. Yang, Y. Sun, C. Dai, Z. Guo, Q. Zhao, F. Zhang and L. Zhu, *Adv. Mater.*, 2025, **37**, 2500236.

68 C. You, L. Tian, J. Zhu, L. Wang, B. Z. Tang and D. Wang, *J. Am. Chem. Soc.*, 2025, **147**, 2010–2020.

69 G. Feng, G. Q. Zhang and D. Ding, *Chem. Soc. Rev.*, 2020, **49**, 8179–8234.

70 W. Li, S. Ai, H. Zhu and W. Lin, *Nat. Commun.*, 2025, **16**, 2471.

71 X. Q. Zhou, P. Wang, V. Ramu, L. Zhang, S. Jiang, X. Li, S. Abyar, P. Papadopoulou, Y. Shao, L. Bretin, M. A. Siegler, F. Buda, A. Kros, J. Fan, X. Peng, W. Sun and S. Bonnet, *Nat. Chem.*, 2023, **15**, 980–987.

72 V. F. Gomerdinger, N. Nabar and P. T. Hammond, *Nat. Rev. Cancer*, 2025, **25**, 657–683.

73 M. J. Baek, D. T. Nguyen, D. Kim, S. Y. Yoo, S. M. Lee, J. Y. Lee and D. D. Kim, *Nat. Nanotechnol.*, 2023, **18**, 945–956.

74 Y. Zhao, Q. Hu, F. Cheng, N. Su, A. Wang, Y. Zou, H. Hu, X. Chen, H. M. Zhou, X. Huang, K. Yang, Q. Zhu, X. Wang, J. Yi, L. Zhu, X. Qian, L. Chen, Y. Tang, J. Loscalzo and Y. Yang, *Cell Metab.*, 2015, **21**, 777–789.

75 (*a*) CCDC 2482027: Experimental Crystal Structure Determination, 2026, DOI: 10.5517/ccdc.csd.cc2p9rd5; (*b*) CCDC 2482032: Experimental Crystal Structure Determination, 2026, DOI: 10.5517/ccdc.csd.cc2p9rkb; (*c*) CCDC 2482033: Experimental Crystal Structure Determination, 2026, DOI: 10.5517/ccdc.csd.cc2p9rlc; (*d*) CCDC 2482034: Experimental Crystal Structure Determination, 2026, DOI: 10.5517/ccdc.csd.cc2p9rmd; (*e*) CCDC 2482035: Experimental Crystal Structure Determination, 2026, DOI: 10.5517/ccdc.csd.cc2p9rnf; (*f*) CCDC 2482036: Experimental Crystal Structure Determination, 2026, DOI: 10.5517/ccdc.csd.cc2p9rpg.